

A COMPARATIVE WMLES STUDY OF THE CRM-HL IN FREE-AIR AND IN THE NTF FACILITY

Victor C. B. Sousa[1], Emre Sozer[2], Kiran Ravikumar[1], Seyedeh Sheida Hosseini[2] & Jared Duensing[2]

[1]Analytical Mechanics Associates, NASA Ames Research Center, Moffett Field, CA 94035
[2]Computational Aerosciences Branch, NASA Ames Research Center, Moffett Field, CA 94035

Abstract

Wall-Modeled Large Eddy Simulation numerical experiments are used as a basis for a comparative analysis of the influence between free-air and the National Transonic Facility (NTF) environments on the NASA High-Lift Common Research Model. The current study was conducted leveraging the Launch, Ascent and Vehicle Aerodynamics (LAVA) unstructured solver and the LAVA Voronoi meshing tool. A discussion on the distributed-memory strategy used in the meshing process is included. An angle-of-attack sweep is performed at $Re_c = 5.49$ million and $Re_c = 12$ million for a 2.7%-scale sting-mounted model and at $Re_c = 5.49$ million for a 5.2%-scale wall-mounted one. Results for the coefficients of lift, drag and moment indicate large differences between the in-tunnel and free-air environments at the $Re_c = 5.49$ million, with stall happening at lower angles inside the NTF. At $Re_c = 12$ million, earlier stall relative to the free-air environment is not observed for the in-tunnel simulations with the full-span sting-mounted 2.7%-scale model. The current results are insufficient to explain the lower lift curve observed in the NTF wind-tunnel experiments using the 5.2% model, when compared to both free-air simulations and data from other experimental facilities.

Keywords: High-Lift Aerodynamics, Wall-Modeled LES, Voronoi Unstructured Meshing

1. Introduction

While Reynolds-Averaged Navier-Stokes (RANS) models are well-suited for cruise conditions characterized by attached flow, they often fail to predict the complex physics at the edges of the flight envelope. One such regime is encountered for take-off and landing maneuvers, where aircraft with fully deployed high-lift devices fly at relatively low-speeds and high angles-of-attack (AOA). Improving computational tools for these configurations is essential for accelerating aircraft certification and reducing developmental costs [1, 2].

Driven by the CFD Vision 2030 Report [3], sustained development efforts by the community as a whole to mature high-fidelity Computational Fluid Dynamics (CFD) have directly enabled the deployment of scale-resolving approaches like Wall-Modeled Large-Eddy Simulations (WMLES). The foundation of WMLES relies on relaxing grid resolution requirements in the near-wall region [4], where the energy-containing scales of the turbulent flow become significantly smaller than those in the freestream. By introducing a wall model to account for the near-wall turbulent shear stress, the mesh can remain coarse near the solid boundary. Meanwhile, the large-scale structures are directly resolved in the freestream, while the remaining subgrid-scale features are modeled. Because of improvements in accuracy, efficiency, and robustness, WMLES has transitioned from an emerging framework into a viable tool for complex engineering applications. Currently, these methodologies are now routinely utilized to predict aerodynamic loads during high-lift maneuvers [5, 6, 7, 8] and in the presence of leading-edge horn-ice [9, 10, 11], as well as to simulate noise levels generated by dual-stream co-axial nozzle jets [12, 13] and turbofans [14].

Within this development context, the High-Lift Prediction Workshop (HLPW) series was established to address the computational shortcomings of simulating takeoff and landing configurations. During the 4th [15] and 5th [16] HLPWs, several independent numerical studies of the NASA High-Lift Common Research Model (CRM-HL) [17] were conducted. Both workshops reached similar outcomes: RANS models struggled to accurately predict stall and flow separation while scale-resolving methods like WMLES demonstrated superior predictive accuracy near stall.
The 5th HLPW included a test case that explored how variations in the Reynolds number affect the aerodynamics of the CRM-HL. The numerical results of this test were expected to be compared against data collected in the National Transonic Facility (NTF) wind tunnel [18] but divergences were found between this dataset and other CRM-HL experiments conducted at the ONERA F1 wind tunnel [19] with a 5.9%-scale full-span model (see Figure 1) and the data was not made available for the 5th workshop [16]. These results were later published by Langston *et al.* [20].

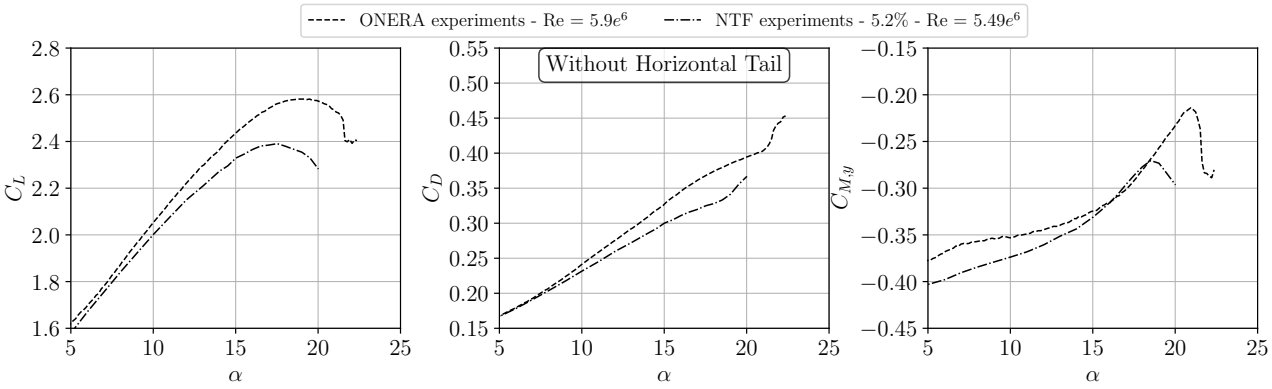


Figure 1 – Different trends exist in experimental aerodynamic coefficient datasets collected at the NTF [20] and ONERA F1 [19] facilities. The presented wind tunnel dataset for the NTF comprises raw aerodynamic measurements that have not undergone wall interference or blockage corrections.

Previous work has been published on simulations performed inside the NTF facility with the wall-mounted semi-span 5.2% high-lift model at $Re_c = 5.49 \times 10^6$ and $Re_c = 30 \times 10^6$. Agrawal *et al.* [21] published their results without seeing the experimental data. They report an increase in lift in the linear regime for the model-in-tunnel simulation in comparison to free-air simulations. Ghate *et al.* [22] performed similar comparisons after the experimental results were published and reported no difference in lift in the linear regime for $Re_c = 5.49 \times 10^6$ but observed the shift for $Re_c = 30 \times 10^6$. In both publications, an earlier stall inside the wind-tunnel was observed and differences between the experimental measurements and the simulated values for the maximum coefficient of lift ($C_{L,\max}$).
Current work aims to compare numerical simulations of the CRM-HL in both free-air and inside the NTF facility with the goal to characterize the impact of the wind-tunnel environment in the search for an explanation for the previously observed discrepancies. WMLES AOA sweeps were conducted at $Re_c = 5.49 \times 10^6$ and $Re_c = 12 \times 10^6$ in free-air and for the 2.7%-scale sting-mounted model inside the NTF wind tunnel. Additionally, a 5.2%-scale wall-mounted half-span model inside the NTF was also considered at $Re_c = 5.49 \times 10^6$. The primary contribution of this work is to assess how the modeled NTF environment modifies CRM-HL aerodynamic loads relative to free-air WMLES. A secondary contribution is the demonstration of a distributed-memory Voronoi meshing workflow that enables large model-in-tunnel simulations with practical turnaround times.

2. Methodology

This work numerically investigates the aerodynamic performance of the CRM-HL, a publicly available geometry developed to foster collaboration [17], in free-air and inside the NTF facility. WMLES were conducted leveraging the LAVA unstructured framework [8, 23]. The numerical scheme is outlined in Section 2.1. The unstructured mesh is built with the LAVA Voronoi meshing tool [24] and an overview of its mesh generation algorithm is included in Section 2.2. Finally, the assumptions made to achieve convergence of the test section conditions in a cost-effective manner in the case of model-in-tunnel

simulations are discussed in Section 2.3.

2.1 Numerical Scheme

The Navier-Stokes equations can be expressed for each unit (control volume) of a discretized domain as,

$$J\frac{\Delta Q}{\Delta t} = \frac{1}{V}\sum_{f=1}^{N_f}(-F_{\mathrm{C}} + F_{\mathrm{D}})A_f, \tag{1}$$

where $Q = (p, u_i, T)$ is the vector containing primitive variables and $W = (\rho, \rho u_i, \rho e)$ is the one containing conserved variables. These quantities are stored at the cell centroids. $J = \frac{\partial W}{\partial Q}$ is the variable transformation Jacobian matrix, $u_i = (u, v, w)$ is the velocity vector, V is the volume of the cell, f represents a cell face, A_f is the area of face f, and N_f is the total number of faces in a cell. Note that this formulation can be used with computational cells that have an arbitrary number of faces. Additionally, the convective and diffusive flux across f are described respectively as,

$$F_C = \begin{bmatrix} \rho u_j n_j \\ \rho u_i u_j n_j + p n_i \\ (\rho e + p) u_j n_j \end{bmatrix} \text{ and } F_D = \begin{bmatrix} 0 \\ \tau_{ij} n_j \\ (\tau_{ji} u_i - q_j) n_j \end{bmatrix}, \tag{2}$$

where τ_{ij} is the viscous stress tensor, q_j is the heat flux vector, and n_i is the face's outward unit normal. A second order accurate formulation is used to compute the fluxes F_C and F_D across the surface f as a function of the primitive variable vector and its gradient evaluated left and right sides of the face f, respectively $Q_{L,R}$ and $\nabla Q_{L,R}$. ∇Q is computed at each cell's centroid using the Green-Gauss method in Sozer *et al.* [25].

The convective flux scheme depends on the evaluation of two fluxes: a centered non-dissipative flux $F_{\mathrm{C}}^{\mathrm{C}}$ and an upwind-biased dissipative flux $F_{\mathrm{C}}^{\mathrm{U}}$. For the centered flux $F_{\mathrm{C}}^{\mathrm{C}}$, we implement an asymptotically entropy conserving and kinetic energy preserving (AEC KEP) flux based on the harmonic mean [26] using left and right cell center values directly. The upwind flux leverages the MUSCL [27] reconstructed primitive variable vectors from either side of the face. After the MUSCL reconstruction, $F_{\mathrm{C}}^{\mathrm{U}}(Q_L, Q_R)$ is computed using the AUSMPW+ [28] flux function.

The two convective fluxes, $F_{\mathrm{C}}^{\mathrm{C}}$ and $F_{\mathrm{C}}^{\mathrm{U}}$ are blended with the aim to achieve low dissipation where turbulence is active and to selectively add appropriate dissipation where compressibility effects are prominent. The final convective flux is expressed as:

$$F_{\mathrm{C}} = (1-\zeta)F_{\mathrm{C}}^{\mathrm{C}} + \zeta F_{\mathrm{C}}^{\mathrm{U}} \tag{3}$$

where ζ is a Ducros [29] type upwind sensor that is computed locally at each face and is used to introduce numerical dissipation in dilatation-dominant regions of the domain. Additional details regarding the construction of the convective and diffusive fluxes can be found in [8, 30].

A Musker-type [31] algebraic equilibrium wall-model coupled with a wall turbulence sensor [8] is used at the wall boundaries to relax the wall-normal spacing requirements and mesh the geometries of interest more efficiently while retaining modeling accuracy. The wall-model exchange location is set as the first cell centroid off the wall and the resulting wall stress is introduced as a viscous flux boundary condition at wall faces. The energy transfer to subgrid-scales is modeled via the constant-coefficient anisotropic Vreman model [32]. Vreman proposed the use of the constant value of $C_v \approx 2.5C_s^2$, where C_s is the Smagorinsky constant. The theoretical value for homogeneous isotropic turbulence is $C_s = 0.17$ which leads to a $C_v = 0.07225$ but, Vreman [32] also recognized that higher values of C_v might be needed for practical applications. In the current work, C_v is set to be 0.08, based on prior studies on canonical turbulence cases as well as practical applications using the LAVA solver [8, 30, 9, 10].

Time integration is carried out using an explicit, third-order strong stability preserving Runge-Kutta scheme [33]. The time step size is the minimum of Δt computed over all cells via:

$$\Delta t = \frac{\mathrm{CFL}}{\sum_{i=x,y,z}(|u_i|S_{xyz,i} + cS_{\mathrm{acoustic}})} \tag{4}$$

where CFL is the Courant–Friedrichs–Lewy number, c is the speed of sound, and the directional and acoustic inverse length scales are defined as:

$$S_{xyz,i} = \frac{\sum_f A_f |n_{f,i}|}{2V}, \quad S_{\text{acoustic}} = \frac{\sum_f A_f}{2V} \tag{5}$$

2.2 Computational Mesh

A Voronoi mesh arises from the subdivision of the computational space Ω via a set of discrete points, also referred to as seeds ($\{s_i\}_{i=1}^N$). Each Voronoi cell (V_i) encompasses the space where all points are closer to its seed (s_i) than any other seed in Ω,

$$V_i = \left\{ \mathbf{x} \in \Omega : \|\mathbf{x} - \mathbf{s}_i\| \leq \|\mathbf{x} - \mathbf{s}_j\|, \quad \text{for all } j \neq i \right\}. \tag{6}$$

These constraints lead to beneficial properties when it comes to the construction of meshes for CFD applications. The resulting faces are planar, oriented orthogonally to the vector joining adjacent seed points, and positioned equidistant from each seed. Such characteristics contribute to smaller interpolation and differentiation errors and enable more accurate and robust finite-volume solvers.
These properties are even better leveraged when regions with regular point distributions are intermingled with smooth transitions in cell size. The governing premise is to maximize the number of cells where error cancellation caused by a regular stencil of neighboring cells lead to inherently well-behaved numerical operators. The seeding and smoothing strategy adopted in LAVA Voronoi meshing tool is described in Sousa *et al.* [24] and a discussion on three different seeding patterns and the resulting benefits and drawbacks can be found in Sozer *et al.* [30].
For WMLES applications, further treatment of the seed points is performed near the solid boundaries. Points within user-prescribed wall-layers are projected to have consistent wall-normal spacing and ensure an equidistant wall-model exchange location [24]. Finally, the body-fitted mesh is generated by subtracting the region inside the input watertight triangulation that describes the geometry of interest. The full clipping process, which is capable of automatic de-featuring and dealing with split cells is described in [24].

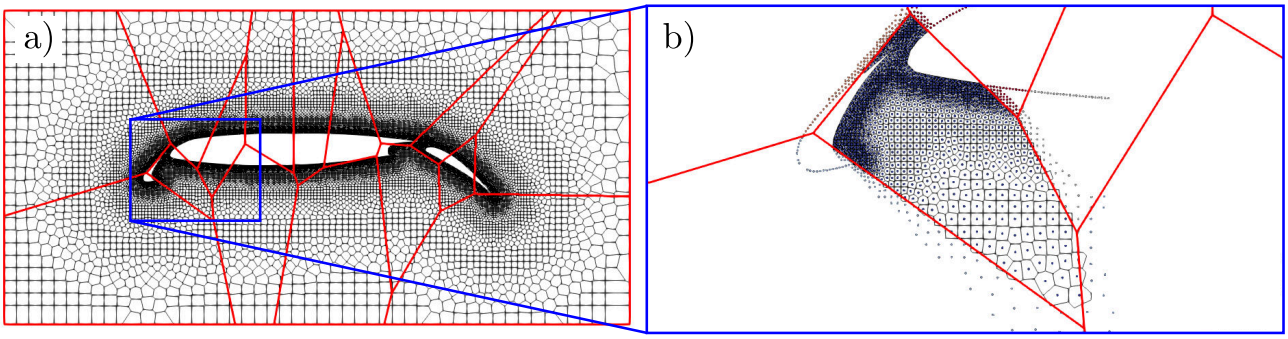


Figure 2 – Example of a Voronoi tessellation used for a distributed-memory parallel mesh generation applied to a two-dimensional multi-element airfoil. **a)** Load-balanced computational domain subdivision into 16 ranks. **b)** Representation of the mesh built within a single rank with both seeds that it owns as well as ghost seeds.

As large-scale WMLES becomes increasingly practical for engineering applications, the ability to generate very large, high-quality meshes has become a critical bottleneck. This is particularly relevant for the NTF model-in-tunnel cases considered here, which require individual meshes for each AOA, each of which with hundreds of millions of cells. Since Sousa *et al.* [24], further development has been made in the LAVA Voronoi mesher. A distributed-memory parallel approach has been introduced based on utilizing a separate Voronoi tessellation of the computational domain to create a partition of the domain with known geometric boundaries. The seed generating points of the partition Voronoi tessellation are initialized randomly but are moved according to the algorithm described in Fu *et al.* [34] to achieve a load-balanced division of the points that are going to form the final mesh (see figure 2). Next, ghost points required to maintain global connectivity in the local rank are identified

and communicated. This is done by extending Peterka *et al.*'s algorithm [35]—originally designed for Cartesian partitions of Ω—to Voronoi cells. After this step, the local meshes are built separately (see figure 2) and are stitched together seamlessly at the writing step.

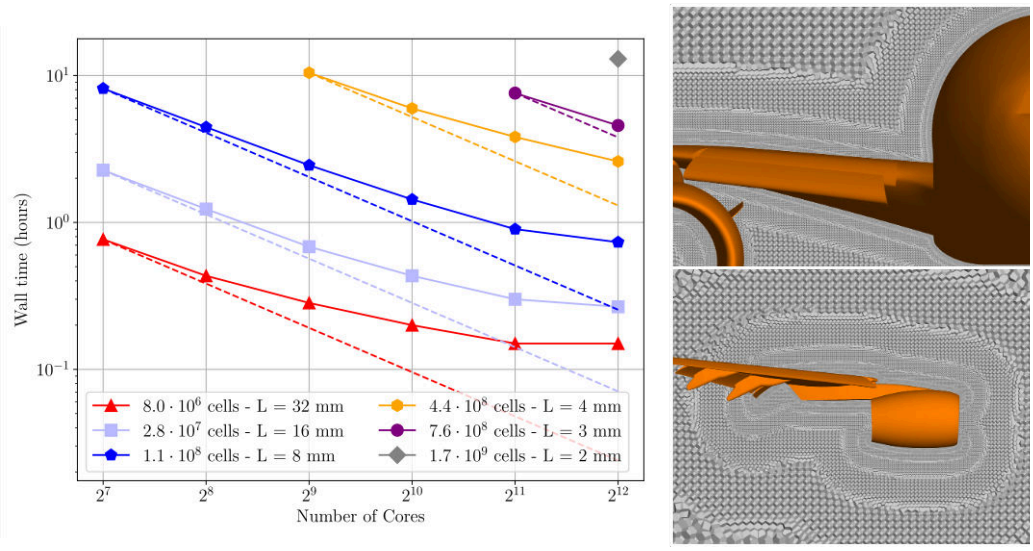


Figure 3 – Scalability of the distributed-memory Voronoi meshing algorithm is shown on the left. Meshes with progressively finer smallest-scale (L) around the CRM-HL were constructed with varying number of cores and their time-to-completion is reported. Tests were performed using AMD Rome nodes with 128 cores each. Example mesh-visualization cuts around the CRM-HL with $L = 32$ mm are shown on the right.

The distributed-memory parallelism has significantly decreased the turnaround time required to create large meshes. For example, a mesh generated for the 5^{th} High-Lift Prediction Workshop (HLPW5), which had its smallest scale set to 4 mm, contains approximately 440 million cells. Using only shared-memory parallelism [24], the wall-clock time required to generate this mesh was approximately 2 days on a single high-memory node. Figure 3 demonstrates that the new approach can generate the same mesh in less than 150 minutes. While this represents a significant reduction in computational time, the contrast is even more pronounced when compared to manual grid generation. For such a geometrically complex configuration, generating structured overset grids was estimated to require approximately two months, or 320 person-hours [36]. Additionally, the new meshing code demonstrates clear scalability, though room for further improvement remains.

Another advantage of Voronoi-based mesh generation is its inherent suitability for parametric analysis, given that the underlying seed distribution can be defined relative to a unified scaling parameter. By varying this control variable, distinct families of meshes can be systematically produced. This parametrization strategy was used to generate the results shown in figure 3. A single mesh definition file was constructed and the only difference between the meshes at different refinement levels is the reference scale, which varied from $L = 32$ mm to $L = 2$ mm.

The automated workflow requires only a closed surface triangulation and a set of user-specified spacing parameters. In the current work, it was chosen to define the cell spacing at the surface and use telescoping regions with a thickness corresponding to 8 cells that double in cell size with increasing distance from the surface. The only exception is at the finest region, which is chosen as a 4-cell-thick-layer. The free-air simulations use the same surface spacing strategy described in [8]. The surface spacing used for the NTF geometry relative to the smallest cell spacing considered in the 5.2% model case is shown in figure 4.

Figure 5 shows slices of coarse unstructured Voronoi meshes for the empty tunnel and model-in-tunnel cases. It shows the concentration of cells near the slot gaps at the top and bottom of the test section walls as well as near the airplane model. When the model is included, the free-air meshing strategy used in Sozer *et al.* [8] for the HLPW5 is superimposed with the empty tunnel strategy depicted in figure 4. It is important to note that the seeding strategy described in Sousa *et al.* [24]

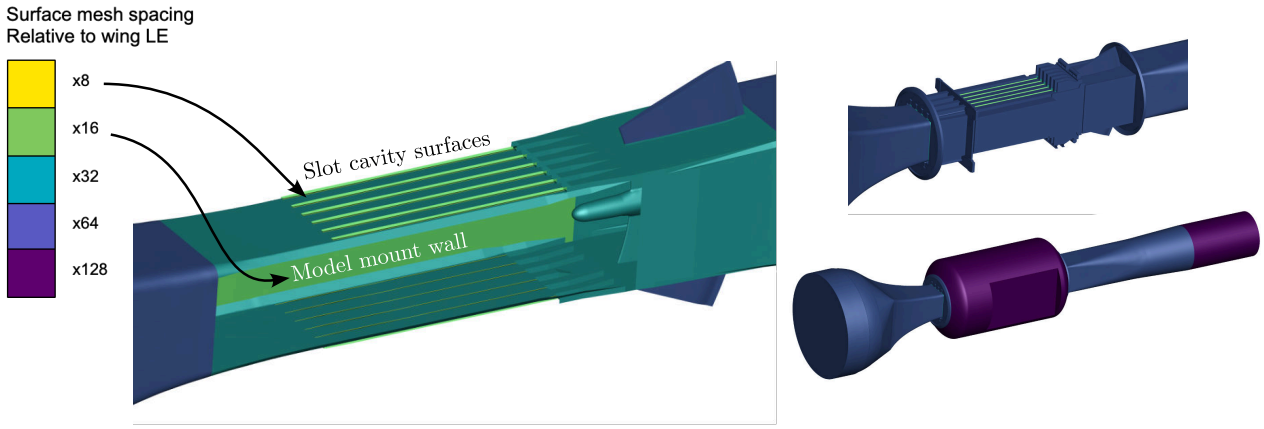


Figure 4 – Relative unstructured surface mesh sizing for NTF relative to 5.2% model.

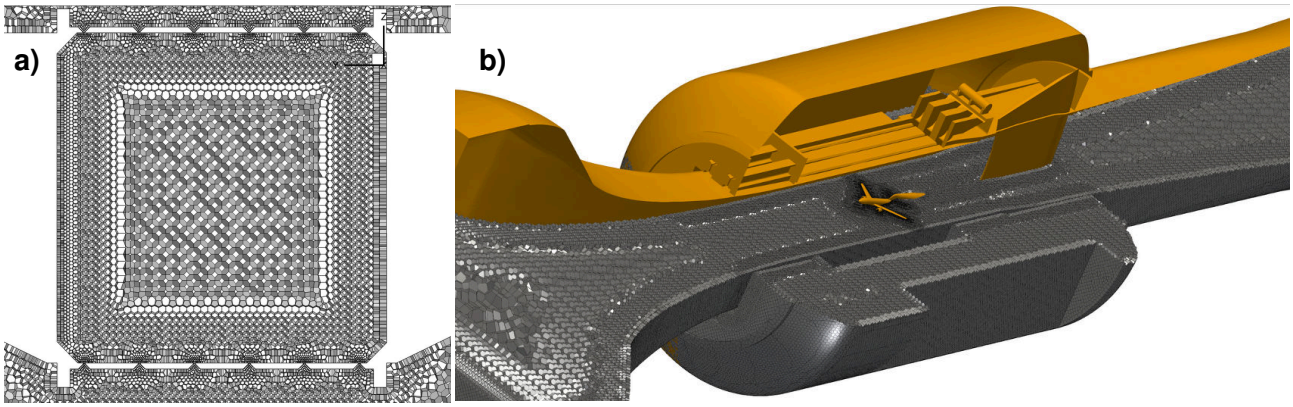


Figure 5 – Coarse representation of the unstructured Voronoi meshes for NTF wind tunnel. **a)** slice of the empty tunnel test section. **b)** 2.7% sting-mounted model-in-tunnel mesh at 19° AOA. Meshes are 8 times coarser than the refinement level used in simulations.

allows for refinement regions to be overlapping, with the region with finest spacing gaining priority over the remaining regions.

In Sozer *et al.* [8], simulated aerodynamic coefficient results were analyzed for three different mesh refinement levels. These meshes had smallest length scales of 8, 6, and 4 mm, which led to 84M, 147M, and 325M cells. It was shown that the finest mesh level (4 mm) agreed well with experimental data and that the medium mesh level (6 mm) produced nearly identical results except at post-stall conditions. In the current work, this information is leveraged, and the meshes generated are consistent with the finest mesh level in Sozer *et al.* [8]. Because the baseline 4 mm reference resolution applies to a full-scale geometry, the cell sizes for the 5.2% and 2.7% models were proportionally scaled down to 0.208 mm and 0.108 mm, respectively, to maintain a constant relative resolution. While the model-specific minimum spacing was reduced, the wind tunnel surface mesh was held constant. Although the grid resolution shown in Figure 4 is defined relative to the minimum spacing of the 5.2% model, this baseline was sufficient to resolve the empty tunnel flow (see Figure 6). Consequently, a deliberate choice was made to maintain the same absolute wind tunnel resolution for the 2.7% model configuration; because the model decreased in size, the resulting wind tunnel surface grid spacing became twice as large relative to the wing leading edge as the baseline spacing described in Figure 4. To mitigate the computational overhead introduced by this refinement, a half-domain simulation with a symmetry boundary condition was performed for the 2.7% model, resulting in a final mesh of approximately 505M cells. In contrast, a symmetry boundary condition was not applicable to the 5.2% wall-mounted half-span model; despite requiring a full-domain simulation, its larger absolute spatial resolution limited the total mesh size to approximately 626M cells.

2.3 Test Section Convergence

Desired test section conditions are calculated based on the Mach number, $M_{ts} = 0.2$, and Reynolds Number based on the MAC ($Re_c = 5.49$ million or $Re_c = 12$ million). The gas is assumed to be air and the test section temperature is set to $T_{ts} = 288.15K$. Assuming total pressure and temperature are conserved, inlet conditions and the first guess for exit static pressure are computed using isentropic relations. The tunnel's initial conditions are chosen to be with a pressure 10% higher than the outlet pressure, to prevent reversed flow during the initial transient. These conditions would be sufficient to conduct accurate inviscid simulations but, for viscous simulations, one needs to account for total pressure loss.

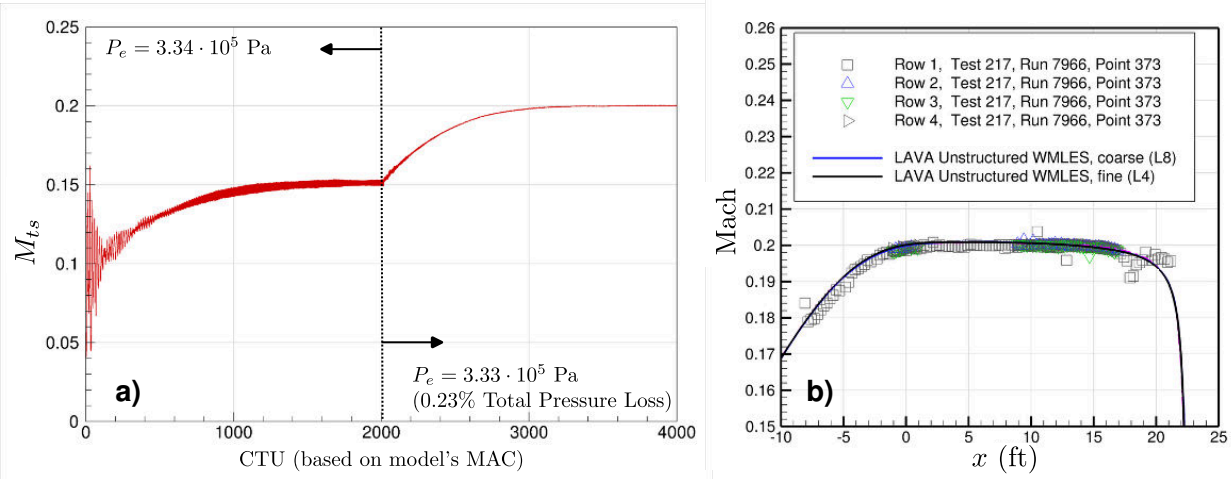


Figure 6 – Empty tunnel simulation results. **a)** Time history of a Mach number probe inside NTF's test section with respect to a CTU relative to the 5.2% model's MAC **b)** Simulated and measured Mach numbers at the center of the empty NTF tunnel.

Empty tunnel simulations—which are computationally cheaper due to a larger allowable time-step size ($\approx 2\mu$s compared to $\approx 8ns$) and a smaller cell count (235M cells compared to 626M cells for the 5.2% model-in-tunnel case)—were used to iteratively adjust the exit static pressure until the desired M_{ts} was attained. An example of a time series of a probe located at the center of the NTF's test section at $x = 13$ ft is shown in figure 6. It shows that, after a transient period that takes approximately 2000 Convective Time Units (CTUs) relative to the 5.2% model's Mean Aerodynamic Chord (MAC), the choice of a lossless pressure at the exit leads to a $M_{ts} \approx 0.15$. Then, P_e is adjusted and a $M_{ts} \approx 0.2$ is achieved. After M_{ts} is converged, the Mach number at the centerline of the simulated NTF tunnel was recorded and compared against experimental measurements and an excellent agreement is obtained. The results shown in Figure 6 are relative to the 5.2% model's test conditions; an identical procedure was conducted for the 2.7% case, though the corresponding results are omitted for brevity. Finally, the empty tunnel conditions are interpolated to meshes that contain the model at different angles of attack and the simulation is run for 90 CTUs based on each model's MAC. After the interpolation, the back pressure remains fixed. For this approach to work, the time window before the model blockage starts affecting the tunnel test section conditions needs to be sufficiently large to wash out interpolation transients and to gather sufficient statistics on the aerodynamic coefficients.

Figure 7 shows the approximate distance from the back of the model to the outlet boundary condition. With this information together with the test section conditions ($M_{ts} = 0.2$ and $T_{ts} = 288.15$ K) it is possible to estimate the time it takes for an acoustic wave to travel the distance from the model to the outlet as well as the minimum time it would take for the model's wake to be advected and reach the outlet. This sequence of events, shown in Table 1, delineates the earliest possible time before aerodynamic blockage effects introduce significant distortions to the test section flow.

In order to assess whether the current methodology is sufficient, it is necessary to check if it is possible to gather accurate estimates for the quantities of interest. For example, if an average operation is performed on the lift coefficient over the stationary portion of the signal, starting at $t^* = t_{\text{avg}} = 30$ CTU, the statistical convergence of this estimate can be inferred by computing the 95% confidence interval

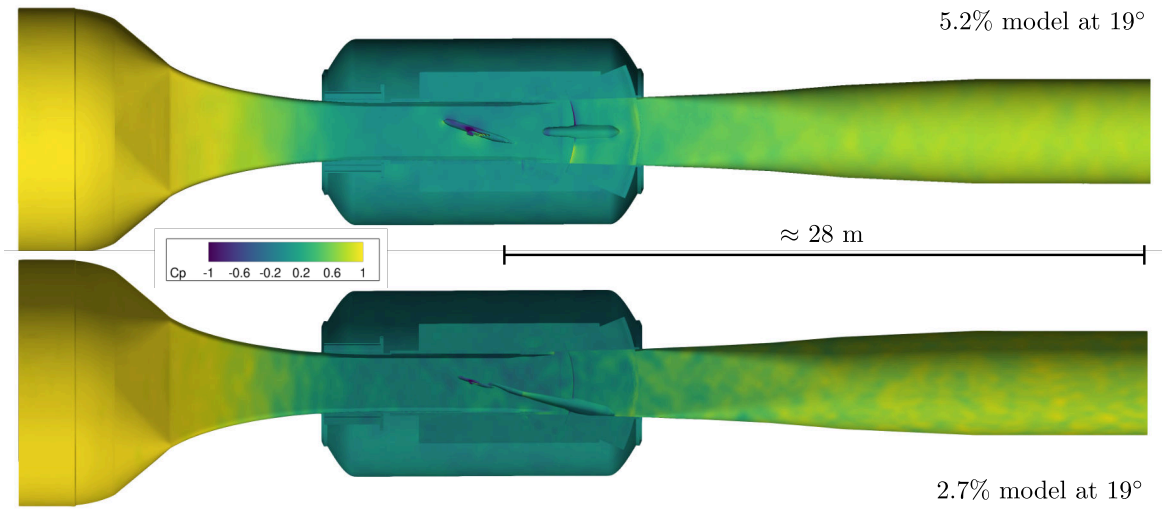


Figure 7 – Illustration of the approximate length scale between the back of the model and the outlet boundary condition in the current simulation campaign for the two different model sizes considered.

Table 1 – Approximate chronological sequence of acoustic and convective events inside the NTF.

Event	**5.2% CTUs**	**2.7% CTUs**
First acoustic wave from the model reaches outlet	15.3	29.6
Acoustic wave's reflection from outlet reaches model	30.6	59.2
Advection of model wake to outlet	76.9	148.0
Acoustic reflection from wake/outlet interaction reaches model	92.2	177.6

(CI) on the mean,

$$\overline{C_L} \pm \frac{1.96\,\sigma}{\sqrt{n_{\text{eff}}}}, \tag{7}$$

where σ is the sample standard deviation over the averaging window and n_{eff} is the effective number of independent samples. Reporting the half-width relative to the mean, $\varepsilon = 1.96\,\sigma/(\sqrt{n_{\text{eff}}}|\overline{C_L}|)$, provides a direct convergence metric: $\varepsilon < 1.5\%$ indicates that the reported mean is statistically converged.

To arrive at a CI, it is necessary to account for the fact that consecutive samples in a time-resolved simulation are not independent. The effective number of independent samples depends on the total length of the averaging window (T_{avg}) and the integrated autocorrelation time (τ_{int}),

$$n_{\text{eff}} = \frac{T_{\text{avg}}}{\tau_{\text{int}}}. \tag{8}$$

The integrated autocorrelation time is defined as

$$\tau_{\text{int}} = \int_0^{s_M} \rho(s)\,ds \approx \Delta s \left(1 + 2\sum_{k=1}^{M} \rho(s_k)\right), \tag{9}$$

where s is the time lag, Δs is the mean sample spacing, $s_k = k\Delta s$, and s_M is the lag at the first zero crossing of ρ. The integrated autocorrelation time depends on the normalized autocorrelation,

$$\rho(s) = \frac{\sum_{t^*}\left(C_L(t^*) - \overline{C_L}\right)\left(C_L(t^*+s) - \overline{C_L}\right)}{\sum_{t^*}\left(C_L(t^*) - \overline{C_L}\right)^2}, \tag{10}$$

which measures how similar the signal is to a time-shifted copy of itself at a lag of s.

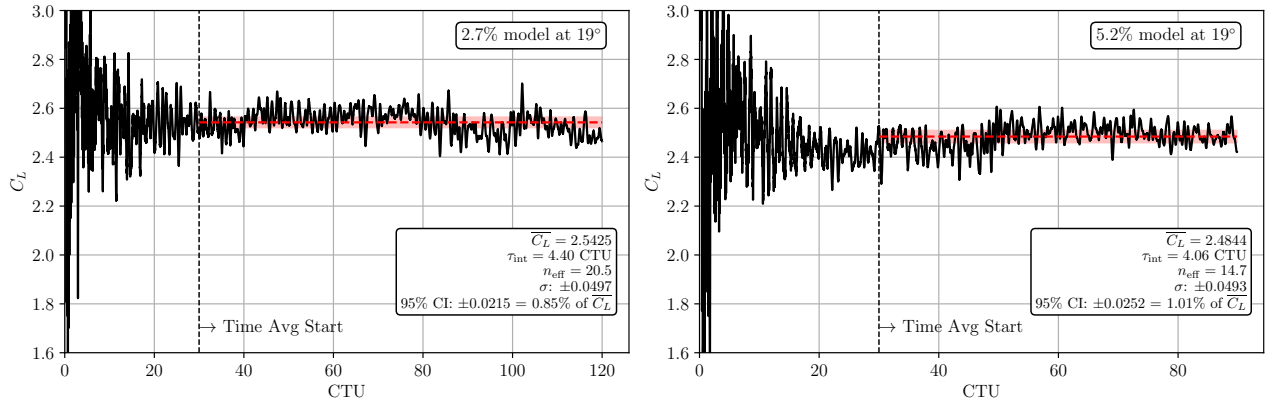


Figure 8 – Time series of the coefficient of lift after interpolation of the converged empty tunnel conditions to model-in-tunnel simulations at 19° of angle of attack. Statistical data indicates convergence of average results within the time window tested.

Lastly, the time series of C_L gathered from numerical simulations of the two different models inside the NTF at 19° angle-of-attack is shown in figure 8. This figure shows evidence that, after the interpolation transient is dissipated, a statistically steady flow is formed where there is enough time, within the window of opportunity, to gather the necessary statistical information on the quantities of interest.c

3. Results

Numerical results are compiled for the CRM-HL in free-air and inside the NTF facility at $Re_c = 5.49 \times 10^6$ and $Re_c = 12 \times 10^6$. Time-averaged force and moment results are analyzed case by case where they are compared against experimental measurements in the NTF and ONERA F1 [19] wind tunnels. To streamline the discussion, the results are shown in three subsections each of which will primarily discuss free-air (3.1) and in-tunnel simulations at $Re_c = 5.49 \times 10^6$ (3.2) and $Re_c = 12 \times 10^6$ (3.3).

3.1 Free-air

Results in figure 9 show that, for all flow conditions and models simulated in a free-air environment, the results for C_L align more closely with the ONERA measurements than those inside the NTF. This set of results also demonstrates that evaluations of the same model at varying Re_c demonstrate that lift scales directly with the Reynolds number across the AOA sweep. Notably, the angle corresponding to $C_{L,\max}$ remains virtually unchanged. As a result, an increased Reynolds number induces an upward shift in the lift curve. This behavior aligns with prior findings such as reported by Sozer *et al.* [8] and Agrawal *et al.* [37].

The small differences in the lift curves observed when the different models were tested at the same environmental conditions are hypothesized to be related to the geometrical differences that exist between the models. The two primary geometric discrepancies consist of the shape of slat attachment on the main wing and the presence of the horizontal tail, which is included in the 2.7% model but not in the 5.2% one. While isolating the horizontal tail contribution from the lift and drag coefficients is straightforward, its physical presence alters the local flow field and significantly modifies the pitching moment coefficient, as seen in top plots in figure 9. These differences are no longer present when plotting the 2.7% model's integrated aerodynamic loads versus the experimental data that includes the horizontal tail wing (see bottom plots in figure 9).

3.2 NTF facility at $Re_c = 5.49 \times 10^6$

Numerical simulations at $Re_c = 5.49 \times 10^6$ were performed with the two different models—at 2.7% and 5.2% scale—inside the NTF wind tunnel and integrated aerodynamic coefficients are plotted in figure 10 for varying angles of attack and are compared against free-air results and experimental measurements.

The numerical model-in-tunnel results for both scales show agreement with each other and with the NTF experimental record with respect to the coefficients of drag (C_D) and pitching moment ($C_{M,y}$).

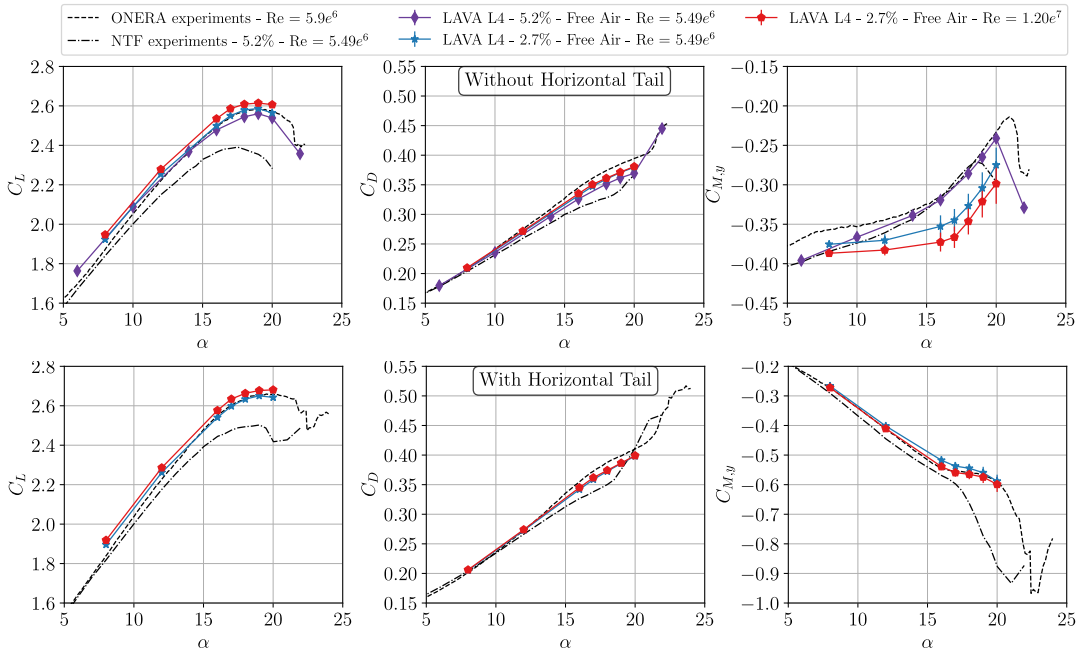


Figure 9 – Time-averaged aerodynamic loads acquired via WMLES of free-air at two different Reynolds numbers compared against measured values at the NTF [20] and ONERA F1 [19] facilities. The presented wind tunnel dataset for the NTF comprises raw aerodynamic measurements that have not undergone wall interference or blockage corrections.

When focus is given to C_L, it can be observed that the simulations inside the NTF for both models predict a stall onset consistent with NTF's experimental data and, therefore, earlier than either the free-air simulations or the ONERA data.
Despite this, the simulated data is not in agreement with the downwards shift observed in the experimental C_L measurements made in the NTF wind tunnel displayed in figure 10. At the lower end on the angle of attack sweep, i.e. with $\alpha \leq 18°$, the C_L gathered from the simulated model-in-tunnel results agree more favorably with free-air simulations and with the ONERA F1 experimental data than with NTF's dataset.
Figure 11 depicts time-averaged pressure profiles for three different stations of the main wing for results gathered during free-air and model-in-tunnel simulations as well as experimental measurements. The depiction of the location of these pressure rows can be found in Section 8.. It can be observed that for lower to intermediate AOA the numerical results for simulations where the model is

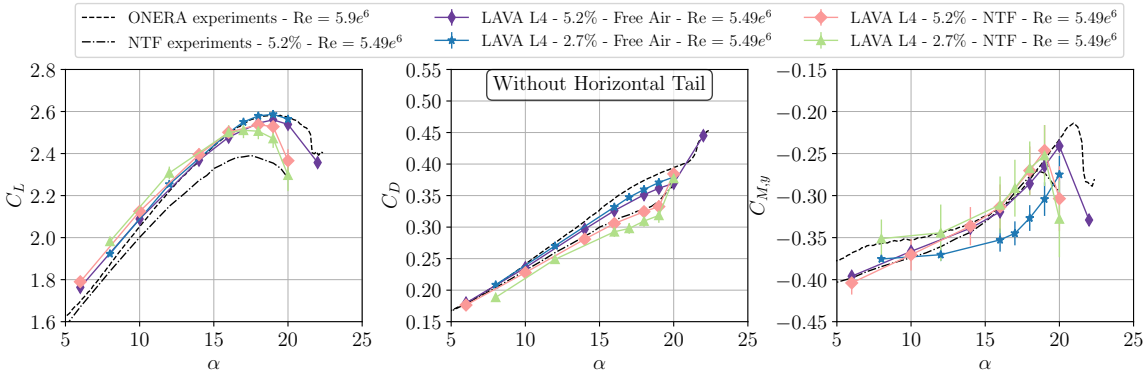


Figure 10 – Time-averaged aerodynamic loads acquired via WMLES of model in NTF at $Re_c = 5.49 \times 10^6$ compared against measured values at the NTF [20] and ONERA F1 [19] facilities. The presented wind tunnel dataset for the NTF comprises raw aerodynamic measurements that have not undergone wall interference or blockage corrections.

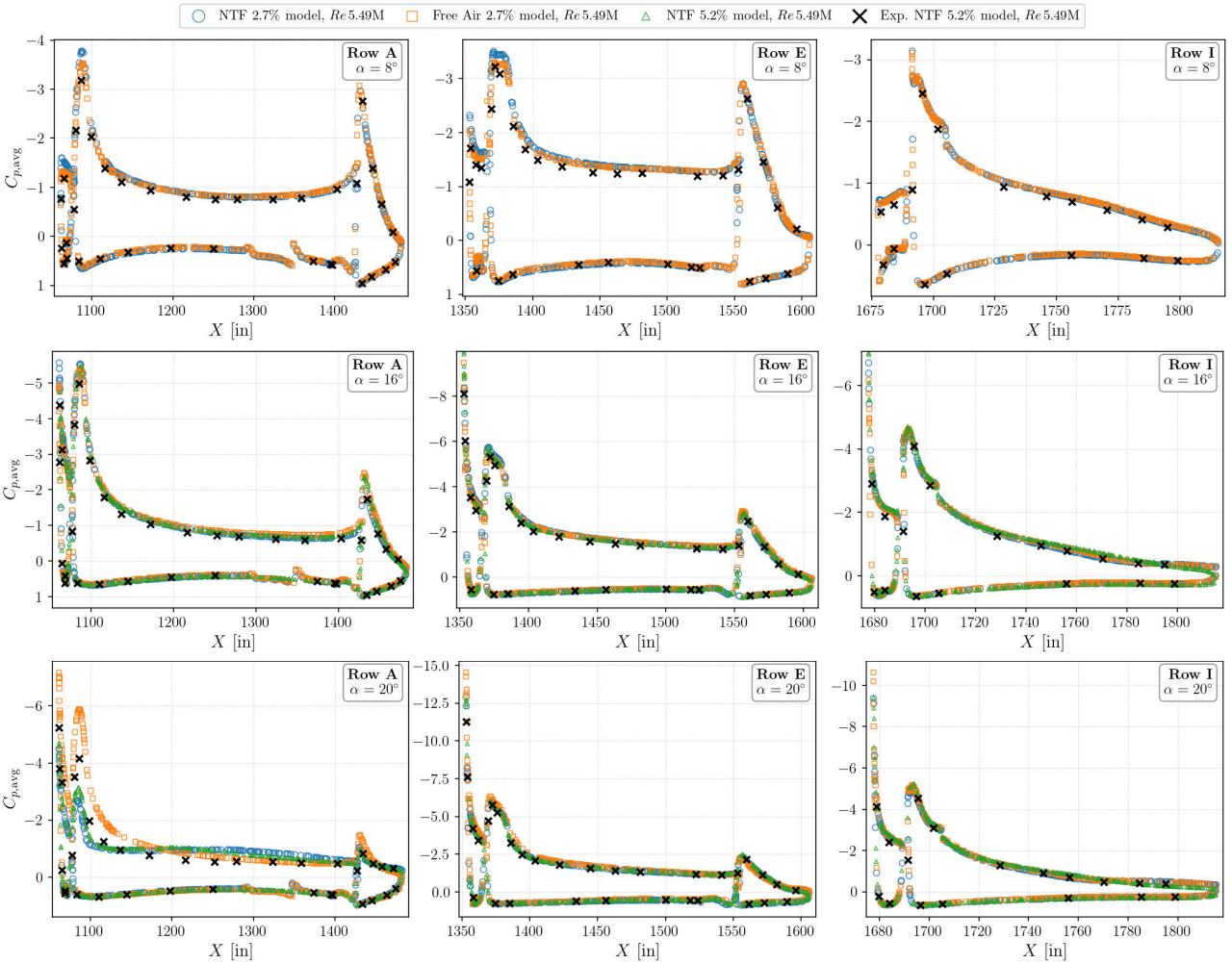


Figure 11 – Time-averaged pressure profiles at row cuts A, E and I, and at different angles of attack. The depiction of the location of these pressure rows can be found in Section 8.. This data was extracted at $Re_c = 5.49 \times 10^6$.

located inside the NTF agree with the data collected in a free-air environment and with experimental measurements. At higher AOA, inboard separation happens in the model-in-tunnel simulations but not in simulations using a free-air environment, evidenced by the lower suction peak at row A at the 20° AOA. The experimental measurements also depict a suction peak lower than free air but not as low as the simulated one for both 5.2% and 2.7% models. Despite the differences observed near the wing root, the mid-board (row E) and outboard (row I) stations show reasonable agreement between the different simulations and the experimental data.

The comparison between the instantaneous axial skin friction coefficient ($C_{f,x}$) field among the different simulations, shown in figure 12, also provides more evidence for the agreement between model-in-tunnel simulations and free-air at low-to-moderate α. It can be observed that at $\alpha = 18^\circ$ the structures of the instantaneous $C_{f,x}$ field are consistent between the different simulations. Additionally, it is possible to observe that the flow remains mostly attached over the wing with the exception of some pizza-shaped separation regions near the outboard of the wing and evidence of the weakening of the flow around the inboard area. On the other hand, at $\alpha = 20^\circ$, the simulations performed inside the NTF display a clear large-scale inboard separation, evidenced by the larger area of low skin friction.

In summary, the inclusion of the NTF's geometry in the simulation has affected the flow and induced an earlier stall consistent with experiments but is not sufficient to explain the divergence between the data obtained via tests in the NTF and ONERA F1 facilities.

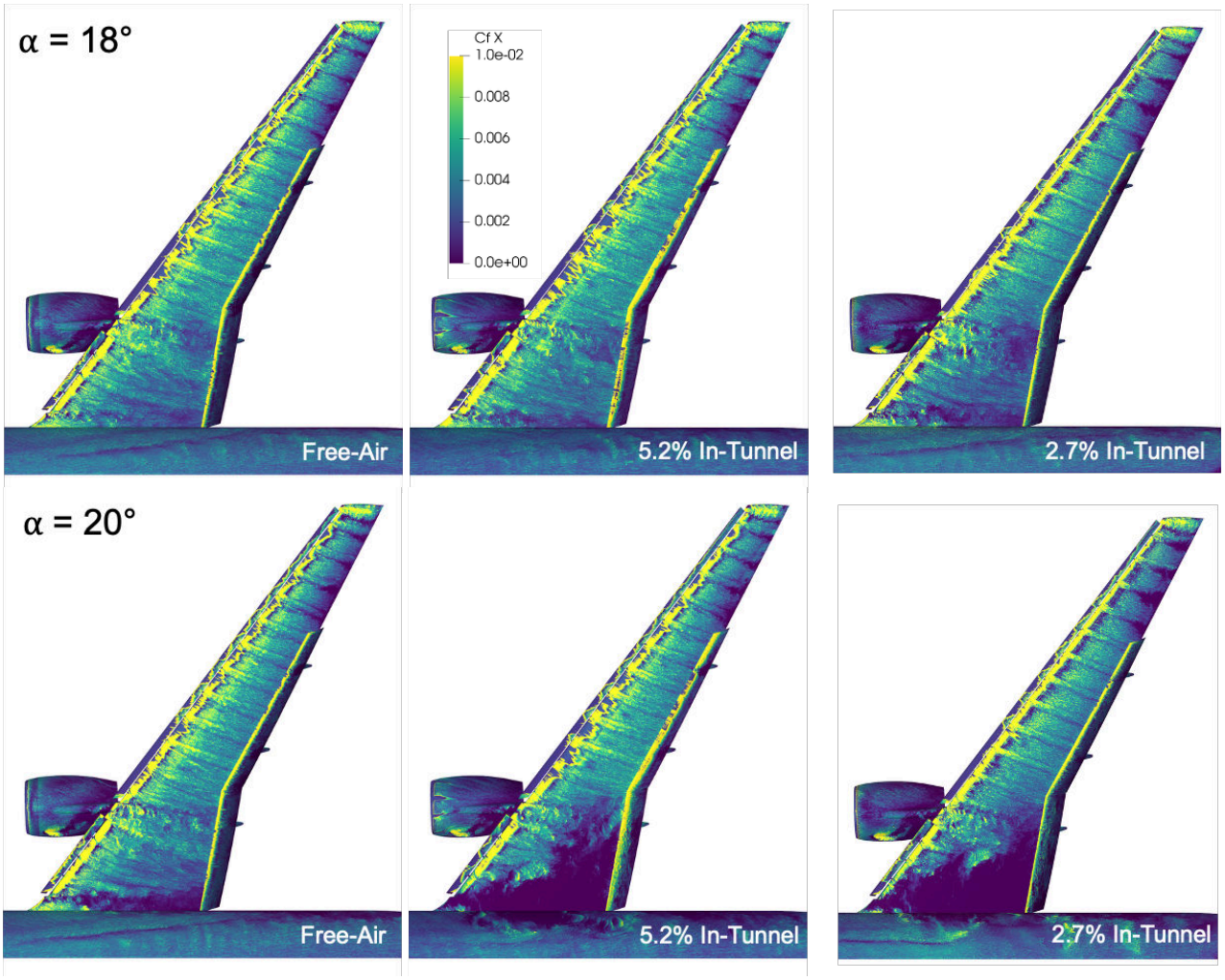


Figure 12 – Instantaneous axial skin friction coefficient at $Re_c = 5.49 \times 10^6$

3.3 NTF facility at $Re_c = 12 \times 10^6$

Numerical simulations of the 2.7% scale model inside the NTF wind tunnel were conducted at $Re_c = 12 \times 10^6$. Figure 13 presents the integrated aerodynamic coefficients across a range of AOA, comparing the computational results against both free-air simulations and experimental measurements.

Results gathered in figure 13 show that the difference in the predicted C_L between free-air and model-in-tunnel simulations is smaller at $Re_c = 12 \times 10^6$ across the angle of attack sweep when compared to the one observed with $Re_c = 5.49 \times 10^6$ (shown in figure 10). This is especially evident in the region close to $C_{L,\text{max}}$. Moreover, figure 13 shows that there is a clear distinction between the drag coefficient simulated in a free-air environment when compared to the one simulated inside the NTF wind tunnel. The former follows the trend of the ONERA F1 wind tunnel experimental dataset more closely while the latter has its parallel with the measurements performed inside the NTF. Similarly to the discussion present in Section 3.1, the removal of the horizontal tail wing's contribution to the integrated pitching moment is not straightforward and the only conclusion that is achievable from results in figure 13 is that there is an influence of the tunnel geometry in the measured $C_{M,y}$, which deviated from the free-air result.

Figure 14 corroborates the conclusion that, at $Re_c = 12 \times 10^6$, the similarities between the free-air and in-tunnel simulations are higher than at $Re_c = 5.49 \times 10^6$. The instantaneous axial skin friction coefficient ($C_{f,x}$) field display similar structures at both $\alpha = 18°$ and $\alpha = 20°$. At the lower angle, similar to figure 12, the flow remains mostly attached with small pizza-shaped separation regions in the outboard region. At the higher angle, differently than at $Re_c = 5.49 \times 10^6$, the inboard section is not fully separated for the in tunnel case.

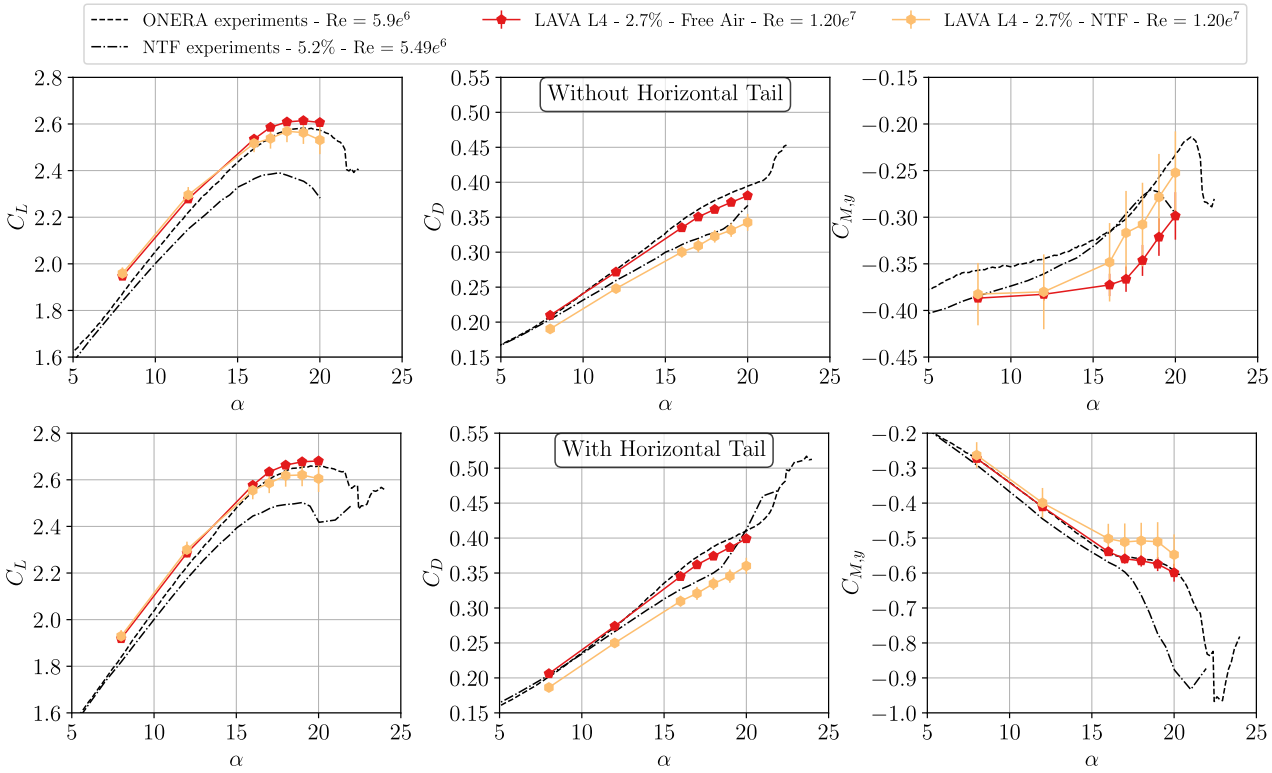


Figure 13 – Time-averaged aerodynamic loads acquired via WMLES of model in NTF at $Re_c = 12 \times 10^6$ compared against measured values at the NTF [20] and ONERA F1 [19] facilities. The presented wind tunnel dataset for the NTF comprises raw aerodynamic measurements that have not undergone wall interference or blockage corrections.

This result differs from previous publications [21, 22], which focused on the flow around the CRM-HL 5.2% model inside the NTF wind tunnel at different Re_c ranging from 5.49×10^6 to 30×10^6. The previously published results indicate that earlier stall inside the wind tunnel when compared to free-air simulations happens at all the tested conditions when using the wall-mounted 5.2% scale model. This suggests that premature-stall behavior may depend on a combination of Reynolds number, model geometry, and installation effects. Additional numerical and experimental studies would be required to isolate the dominant mechanism.

4. Summary

This study leveraged a framework encompassing the LAVA unstructured solver and the LAVA Voronoi mesher to conduct WMLES numerical experiments for two different CRM-HL models in both free-

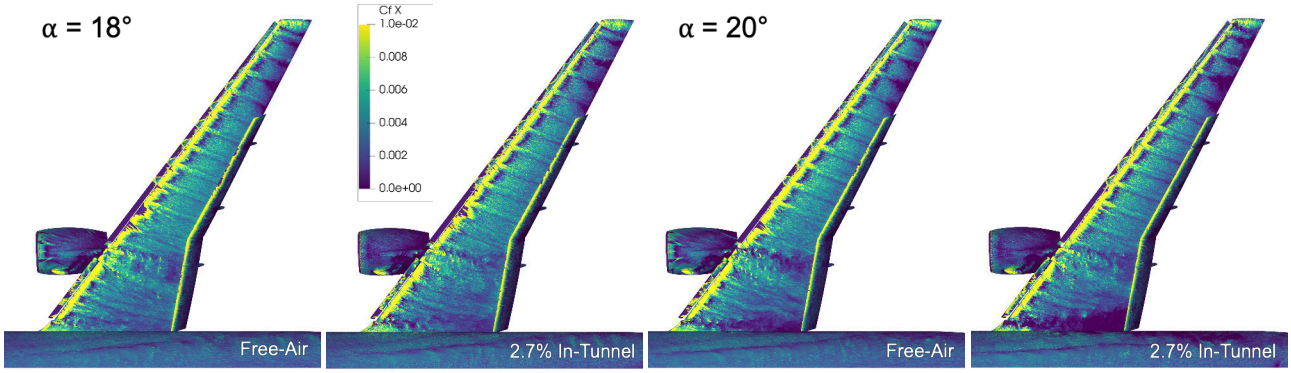


Figure 14 – Instantaneous axial skin friction coefficient at $Re_c = 12 \times 10^6$

air and NTF wind-tunnel environments. The underlying numerical scheme and meshing strategy were presented, alongside an overview of the distributed-memory meshing algorithm. This parallel computing approach successfully eliminated prior memory limitations and demonstrated scalability that reduced production mesh generation times from approximately two days to under three hours. Additionally, the methodology and validity of using empty tunnel simulations to converge test section conditions were evaluated.

Numerical simulations were performed for a wall-mounted, half-span 5.2% model and a sting-mounted, full-span 2.7% model. The test matrix included Reynolds numbers of $Re_c = 5.49 \times 10^6$ and 12×10^6 for the 2.7% model, and $Re_c = 5.49 \times 10^6$ for the 5.2% model. The resulting data highlighted the differences between the free-air and in-tunnel environments. At $Re_c = 5.49 \times 10^6$, both model scales exhibited earlier stall and a lower $C_{L,\max}$ inside the wind tunnel compared to free-air configurations. This trend aligns with previously published simulations of the 5.2% wall-mounted model [21, 22]. However, unlike the 5.2% model where earlier stall was ubiquitous across the Re_c range of 5.49×10^6 to 30×10^6 [21, 22], the 2.7% sting-mounted model did not exhibit premature stall at $Re_c = 12 \times 10^6$. This discrepancy suggests that distinct aerodynamic mechanisms may drive the premature stall behaviors observed across different model scales and mounting strategies but further numerical and experimental studies are needed to better support this hypothesis.

Ultimately, the current set of simulations is not sufficient to fully explain the divergence between experimental measurements performed at the ONERA F1 wind tunnel [19] and the ones gathered inside the NTF [20]. The constant shift to lower values in the coefficient of lift observed in the NTF experiments when compared to the ONERA or free-air results are not reflected in the numerical simulations presented in the current work. Further numerical and experimental work is needed to characterize the causes behind these observed differences. A similar conclusion was also reached in [22].

5. Contact Author Email Address

Please address Victor Sousa at: victor.decarvalhobrittosousa@nasa.gov

6. Copyright Statement

The authors confirm that they, and/or their company or organization, hold copyright on all of the original material included in this paper. The authors also confirm that they have obtained permission, from the copyright holder of any third party material included in this paper, to publish it as part of their paper. The authors confirm that they give permission, or have obtained permission from the copyright holder of this paper, for the publication and distribution of this paper as part of the ICAS proceedings or as individual off-prints from the proceedings.

7. Acknowledgments

This research is sponsored by the NASA Transformational Tools and Technologies (TTT) Project of the Transformative Aeronautics Concepts Program (TACP) under the Aeronautics Research Mission Directorate (ARMD). Computational resources supporting this work were provided by the NASA High-End Computing (HEC) Program through the NASA Advanced Supercomputing (NAS) Division at Ames Research Center. The authors would like to thank Brandon Lowe and Gerrit-Daniel Stich for their review and essential feedback on this paper.

8. Appendix

Figure 15 shows the pressure-row locations requested for HLPW5 data comparisons.

References

[1] Jeffrey P Slotnick and Dimitri Mavriplis. A grand challenge for the advancement of numerical prediction of high lift aerodynamics. In *AIAA Scitech 2021 Forum*, page 0955, 2021.

[2] Timothy Mauery, Juan Alonso, Andrew Cary, Vincent Lee, Robert Malecki, Dimitri Mavriplis, Gorazd Medic, John Schaefer, and Jeffrey Slotnick. A guide for aircraft certification by analysis. Technical report, National Aeronautics and Space Administration, 2021.

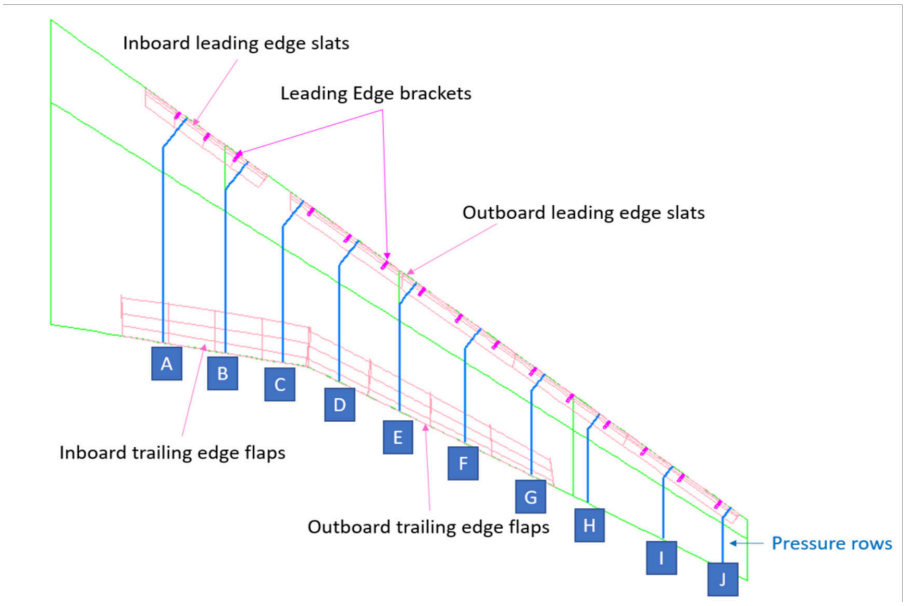


Figure 15 – Location of pressure rows on the wing of the CRM-HL.

[3] Jeffrey P Slotnick, Abdollah Khodadoust, Juan Alonso, David Darmofal, William Gropp, Elizabeth Lurie, and Dimitri J Mavriplis. CFD vision 2030 study: a path to revolutionary computational aerosciences. Technical report, NASA, 2014.

[4] Haecheon Choi and Parviz Moin. Grid-point requirements for Large Eddy Simulation: Chapman's estimates revisited. *Physics of fluids*, 24(1), 2012.

[5] Konrad A Goc, Oriol Lehmkuhl, George Ilhwan Park, Sanjeeb T Bose, and Parviz Moin. Large Eddy Simulation of aircraft at affordable cost: a milestone in computational fluid dynamics. *Flow*, 1:E14, 2021.

[6] Cetin C Kiris, Aditya S Ghate, Jared C Duensing, Oliver M Browne, Jeffrey A Housman, Gerrit-Daniel Stich, Gaetan Kenway, Luis S Fernandes, and Leonardo M Machado. High-lift common research model: RANS, HRLES, and WMLES perspectives for CLmax prediction using LAVA. In *AIAA SciTech 2022 Forum*, page 1554, 2022.

[7] Li Wang, William K Anderson, Eric J Nielsen, Ponnampalam Balakumar, Michael A Park, Jan-Renee Carlson, Prahladh S Iyer, and Boris Diskin. Wall-Modeled Large-Eddy Simulations for high-lift configurations using FUN3D. In *AIAA SciTech 2022 Forum*, page 1555, 2022.

[8] Emre Sozer, Michael F Barad, Jeffrey A Housman, Francois Cadieux, Victor Sousa, Ercan Dumlupinar, Kumar Saurabh, Kiran Ravikumar, and Jared C Duensing. LAVA WMLES results for the 5th high-lift prediction workshop. In *AIAA Scitech 2025 Forum*, page 0887, 2025.

[9] David Craig Penner, Victor C B Sousa, Kiran Ravikumar, Kumar Saurabh, Francois Cadieux, Gerrit-Daniel Stich, Michael F Barad, Jeffrey A Housman, and Jared C Duensing. Wall-Modeled LES of a swept wing with leading-edge ice using LAVA curvilinear, unstructured, and cartesian solvers. In *AIAA SCITECH 2025 Forum*, page 0059, 2025.

[10] David A Craig Penner, Victor CB Sousa, Jeffrey A Housman, Kiran Ravikumar, Gerrit-Daniel Stich, and Jared C Duensing. Large-Eddy Simulation of an iced swept wing: A perspective on the aerodynamic effect of triggering resolved turbulence. Technical report, National Aeronautics and Space Administration, 2025.

[11] Brett Bornhoft, Parviz Moin, Suhas S Jain, and Sanjeeb T Bose. On the use of artificial ice shapes for Large-Eddy Simulations in aircraft icing. *Journal of Aircraft*, 62(5):1240–1257, 2025.

[12] Guillaume A Bres, Sanjeeb T Bose, Michael Emory, Frank E Ham, Oliver T Schmidt, Georgios Rigas, and Tim Colonius. Large-Eddy Simulations of co-annular turbulent jet using a Voronoi-based mesh generation framework. In *2018 AIAA/cEAS aeroacoustics conference*, page 3302, 2018.

[13] Gerrit-Daniel Stich, Aditya S Ghate, Jeffrey A Housman, and Cetin C Kiris. Wall-Modeled Large-Eddy Simulation of jet noise in flight conditions. In *28th AIAA/CEAS Aeroacoustics 2022 Conference*, page 3002, 2022.

[14] Guillaume A Brès, Kan Wang, Christopher B Ivey, Sanjeeb Bose, Gaku Okubo, Toshihiro Kamatsuchi, and Hisato Tanaka. GPU-accelerated Large-Eddy Simulations for aeroacoustic predictions of a full-wheel multi-stage turbofan engine. In *AIAA AVIATION FORUM AND ASCEND 2025*, page 3653, 2025.

[15] Christopher L Rumsey, Jeffrey P Slotnick, and Carolyn D Woeber. Fourth high-lift prediction/third ge-

ometry and mesh generation workshops: Overview and summary. *Journal of Aircraft*, 60(4):1160–1177, 2023.

[16] Adam M Clark, Chris Rumsey, Jeffrey P Slotnick, and Li Wang. HLPW-5: Overview and workshop summary. In *AIAA SciTech Forum*, 2025.

[17] Doug S Lacy and Adam M Clark. Definition of initial landing and takeoff reference configurations for the high lift common research model (CRM-HL). In *AIAA Aviation 2020 Forum*, page 2771, 2020.

[18] Brent W Pomeroy, Melissa B Rivers, Scott Brynildsen, Norma Farr, Ben J Rider, and Seyedeh Sheida Hosseini. National Transonic Facility public geometry release and summary. In *AIAA Aviation Forum And Ascend 2025*, page 3160, 2025.

[19] Sylvain Mouton, Grégoire Charpentier, and Annabelle Lorenski. Test summary of the full-span high-lift common research model at the ONERA F1 pressurized low-speed wind tunnel. In *AIAA Scitech 2023 Forum*, page 0823, 2023.

[20] Sarah Langston, Courtney S Winski, and Melissa B Rivers. Reynolds number effects on a 5.2%-scale high lift common research model. In *AIAA Scitech 2025 Forum*, page 1514, 2025.

[21] Rahul Agrawal, Michael Whitmore, Sanjeeb Bose, and Parviz Moin. Investigations of wind-tunnel effects in Large-Eddy Simulations of the NTF high-lift common research model aircraft. In *AIAA Scitech 2025 Forum*, page 0058, 2025.

[22] Aditya S Ghate, Jordan B Angel, Gaetan Kenway, Man Long Wong, and Cetin C Kiris. Large Eddy Simulations of high-lift common research model in the NTF wind tunnel at flight scale reynolds numbers. In *AIAA Scitech 2026 Forum*, page 0020, 2026.

[23] Michael Barad, Emre Sozer, Jeffrey Housman, Jared Duensing, Alexander Aghili, Josh Anibal, Chase Ashby, Austin Bell, Francois Cadieux, Timothy Chau, et al. Launch Ascent and Vehicle Aerodynamics (LAVA) a NASA mission-critical CFD solution-gearing up for public release. In *Advanced Modeling and Simulation (AMS) Seminars*, 2025.

[24] Victor Sousa, Abram K Rodgers, Keshav Sriram, Emre Sozer, Michael F Barad, Gerrit-Daniel Stich, Francois Cadieux, and Jared Duensing. LAVA Voronoi mesher for Wall-Modeled Large-Eddy Simulations. In *AIAA Aviation Forum 2024*, page 4306, 2024.

[25] Emre Sozer, Christoph Brehm, and Cetin C Kiris. Gradient calculation methods on arbitrary polyhedral unstructured meshes for cell-centered CFD solvers. In *52nd Aerospace Sciences Meeting*, page 1440, 2014.

[26] Carlo De Michele and Gennaro Coppola. Asymptotically entropy-conservative and kinetic-energy preserving numerical fluxes for compressible euler equations. *Journal of Computational Physics*, 492:112439, 2023.

[27] Bram van Leer. Towards the ultimate conservative difference scheme. ii. monotonicity and conservation combined in a second-order scheme. *Journal of Computational Physics*, 14:361–370, 03 1974.

[28] Kyu Hong Kim, Chongam Kim, and Oh-Hyun Rho. Methods for the accurate computations of hypersonic flows: I. ausmpw+scheme. *Journal of Computational Physics*, 174(1):38–80, 2001.

[29] F Ducros, V Ferrand, F Nicoud, C Weber, D Darracq, C Gacherieu, and T Poinsot. Large-eddy simulation of the shock/turbulence interaction. *Journal of Computational Physics*, 152(2):517–549, 1999.

[30] Emre Sozer, Aditya S Ghate, Gaetan K Kenway, Michael F Barad, Victor C Sousa, and Cetin C Kiris. Evaluation of Voronoi meshes for large eddy simulations of high lift aerodynamics. In *AIAA Scitech 2023 Forum*, page 0255, 2023.

[31] Antony J Musker. Explicit expression for the smooth wall velocity distribution in a turbulent boundary layer. *AIAA journal*, 17(6):655–657, 1979.

[32] AW Vreman. An eddy-viscosity subgrid-scale model for turbulent shear flow: Algebraic theory and applications. *Physics of fluids*, 16(10):3670–3681, 2004.

[33] Sigal Gottlieb, Chi-Wang Shu, and Eitan Tadmor. Strong stability-preserving high-order time discretization methods. *SIAM review*, 43(1):89–112, 2001.

[34] Lin Fu, Xiangyu Y Hu, and Nikolaus A Adams. A physics-motivated centroidal voronoi particle domain decomposition method. *Journal of Computational Physics*, 335:718–735, 2017.

[35] Tom Peterka, Dmitriy Morozov, and Carolyn Phillips. High-performance computation of distributed-memory parallel 3D Voronoi and Delaunay tessellation. In *SC'14: Proceedings of the International Conference for High Performance Computing, Networking, Storage and Analysis*, pages 997–1007. IEEE, 2014.

[36] Aditya S Ghate, Gaetan KW Kenway, Gerrit-Daniel Stich, Daniel Maldonado, and Cetin C Kiris. A Wall-Modeled LES perspective for the high lift common research model using LAVA. In *AIAA Aviation Forum and Exposition 2022*, 2022.

[37] Rahul Agrawal, Michael Whitmore, Konrad Goc, Sanjeeb Bose, and Parviz Moin. Reynolds number sensitivities in Wall-Modeled Large-Eddy Simulation of a high-lift aircraft. In *AIAA Aviation Forum And Ascend 2024*, page 4174, 2024.